Solution-based Cu+ transient species mediate the reconstruction of copper electrocatalysts for CO2 reduction

nature catalysis

Article

https://doi.org/10.1038/s41929-023-01070-8

Solution-based Cu^+ transient species mediate the reconstruction of copper electrocatalysts for CO_2 reduction

In the format provided by the authors and unedited

Catalyst characterization

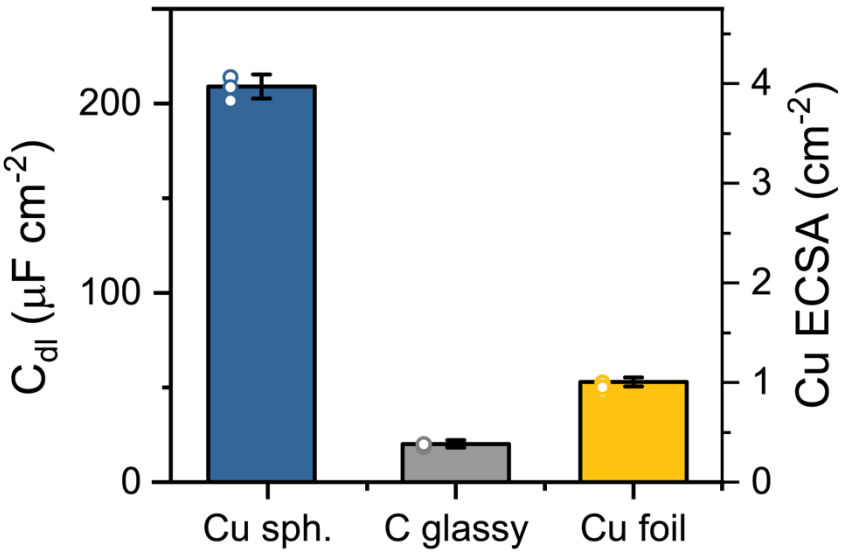

Supplementary Figure 1: ECSA (electrochemically active surface area) expressed as cm^{-2} of Cu surface in per 1 cm^{-2} of geometric electrode surface area calculated from double layer capacitance (C_{dl}) measurements. Electropolished Cu foil was used to normalize the ECSA for Cu nanoparticle films. Data are the mean of 3 independent measurements and the error bar represents the estimated standard deviation on the same.

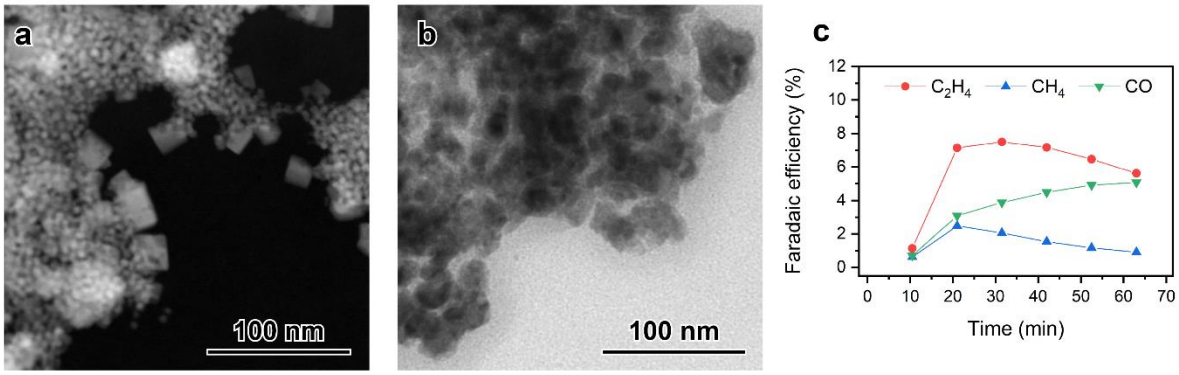

Supplementary Figure 2: Catalyst characterization post-electrolysis. (a) High angle annular dark field scanning TEM image of the catalyst after 5 min of chronoamperometry at –1.2 V_{RHE}. The spherical primary particles are accompanied by redeposited larger cube-shaped secondary particles. (b) Bright field TEM image of the catalyst after 60 min of chronoamperometry at –1.2V_{RHE}. All primary particles have transformed into redeposited secondary particles. (c) Faradaic efficiency of the catalyst during the first 60 min of CO_2RR.

The electrochemical measurements were performed using a Biologic SP-300 potentiostat. Ambient pressure CO_2 electrolysis was carried out in a custom-made gas-tight electrochemical cell made of poly-carbonate and fitted with Buna-N O-rings built in our laboratory and used in previous studies. The configuration of the electrochemical cell is such that the working electrode sits parallel with respect to the counter electrode to ensure a uniform potential distribution across the surface. A Selemion AMV anion exchange membrane is used to separate the anodic and cathodic compartments. 0.1 M $KHCO_3$ solution was used as electrolyte. During electrolysis, CO_2 was constantly bubbled through the electrolyte at a flow rate of 5 sccm to prevent depletion of CO_2 in the electrolyte and allow continuous analysis of gaseous products via a gas chromatograph. The flow rate of CO_2 was controlled with a mass flow controller (Bronkhorst), and the gas was first humidified with water by passing it through a bubbler to minimize evaporation of electrolyte. A platinum foil was used as the counter electrode and Ag/AgCl electrode (leak free series) from Innovative Instruments, Inc. was used as the reference electrode. For the analysis of gaseous products, a gas chromatograph (GC, SRI instruments) equipped with a HayeSep D porous polymer column, thermal conductivity detector, and flame ionization detector was used. Ultra-high purity N_2 (99.999%) was used as a carrier gas. The concentration of gaseous products was determined using calibration curves from standard gas mixtures.

On-line ICP-MS measurements

Supplementary Note 1: Optimization of electrochemical protocols

A previous study shows that Cu transiently dissolves at OCP.[1] This means that Cu is not stable under OCP conditions, and especially in the presence of O_2. Similar dissolution behavior is observed when the spherical Cu NPs are in contact with the electrolyte at OCP without (Figure 3a) or with the dmphen (Figure 3b) When the potential is decreased to 0 V_{RHE}, Cu dissolution decreases and reaches the baseline of the Cu signal.

This observation indicates that the bulk Cu concentration under CO_2RR conditions is negligible compared to the dissolution at OCP and the latter masks the visibility of the signal of interest. Therefore, the on-line ICP MS protocol was modified so that the contact with the working electrode was established applying either a potential below 0 V_{RHE} or mild negative current densities. –0.28 mA cm^{-2} was identified as the optimal value.

We note that a rapid 'cell failure' was observed when holding the potential below –1.1V_{RHE}, where CO_2RR typically occurs, due to vigorous bubble formation. The formed bubbles block the inlet channel of the scanning flow cell and the capillary through which the reference electrode is connected to the cell, resulting in contact loss. Thus, a galvanostatic electrochemical protocol was established to make the measurements more reliable. Additionally, the length of current pulses at more negative current densities was maintained relatively short (less than a minute). In this way, the kinetics of bubble formation was better controlled.

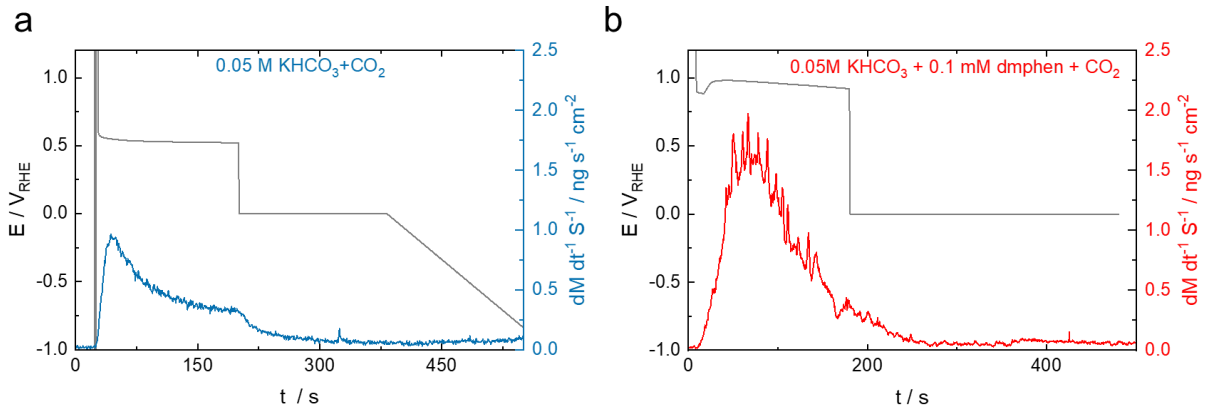

Supplementary Figure 3: Dissolution profiles with contact at OCP collected for the Cu NPs. Measurements were performed in (a) 0.05 M $KHCO_3$ solution and (b) 0.05 M $KHCO_3$ + 0.1 mM dmphen solution. Both solutions were saturated with CO_2 and Ar. The electrochemical

protocol consisted of three parts; contact with the working electrode was established under open circuit conditions. After three minutes the potential was shifted to 0 V_{RHE} for an additional three minutes (no phenanthroline in the electrolyte) and five minutes (0.1 mM dmphen in the electrolyte). The protocol was ended with a slow potential ramp (only partially shown) from 0 V_{RHE} to –1 V_{RHE} applying 5 mV s^{-1} scan rate.

Detection of Cu ions via optical spectroscopy

Supplementary Note 2: Discussion on the choice of the phenanthroline ligand and optical quantification of the Cu species in the electrolyte.

Ligands derived from the 1,10-phenanthroline enable the detection of Cu(I) species because the associated complexes exhibit a MLCT (Metal to Ligand Charge Transfer band).[2,3,4] One of the requirements of the phenanthroline ligand for the optical detection in this study was water solubility because an aqueous electrolyte is used in CO_2RR. We screened different phenanthroline ligands and found that only the parent 1,10-phenanthroline (phen) and 2,9-dimethyl-phenanthroline (dmphen) meet this criterion. We synthesized the complexes of these ligands with Cu^+ in a ligand:Cu 2:1 ratio following reported methods.[3] These complexes obtained in the solid form were first dissolved in ethanol at 1 mM concentration. Further dilutions to perform the optical measurements in Supplementary Figure 4 were performed with water. We note that $[Cu(phen)_2]^+$ rapidly oxidises in water at the concentration range used in this work in the absence of a stabilizer (sodium ascorbate). Instead, the $[Cu(dmphen)_2]^+$ remains stable without a stabilizer. The steric impediment of the methyl groups towards the geometry change occurring when switching from Cu^+ to Cu^{2+} complexes explains the stability of $[Cu(dmphen)_2]^+$ versus $[Cu(phen)_2]^+$.[4,5] Furthermore, Supplementary Figure 4a evidences the more intense absorption of the MLCT band of the dmphen complex compared to the phen for the same concentration, which implies higher sensitivity towards Cu ion detection. The higher stability in water and the higher absorption of the dmphen complex prompted us to use the dmphen ligand in the optical detection.

Supplementary Figure 4b report the calibration curve for dmphen complexes from which a molar absorption coefficient ϵ_{454}=5700 $M^{-1}cm^{-1}$ at λ_{max}= 454 nm was determined. We note that the lowest concentration of Cu^+ that could be reliably and confidently detected with the dmphen complex is 1 µM, corresponding to an absorbance of 0.0054. We considered this value as the detection limit of the method for further tests.

To validate our calibration, we checked that no $[Cu(dmphen)_2]^+$ was actually converted into $[Cu(dmphen)_2]^{2+}$ during the measurements by monitoring its absorption over time when the vial containing the solution was left open to air. We measured a less than 1% decrease in the absorbance after 10 minutes. In our experiments, the UV-vis spectra are acquired within 5 minutes following the collection of the aliquots, thus we can confidently state that the $[Cu(dmphen)_2]^+$ complex is stable at the timescales used in this study.

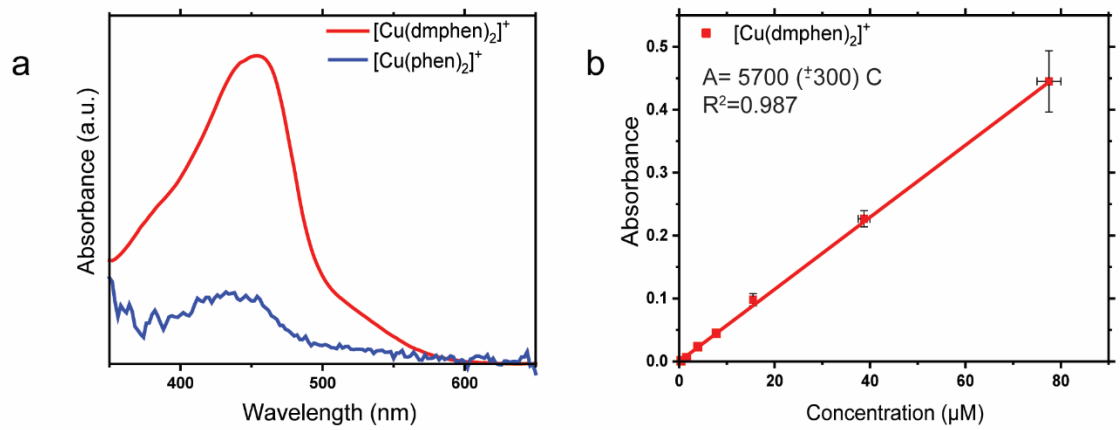

Supplementary Figure 4: (a) Absorbance spectra for the Cu^+ complexes obtained with 1,10-phenanthroline (blue curve) and 2,9-dimethyl-1,10-phenanthroline (red curve) in a 0.1 mM solution in water. (b) Calibration curve correlating the MLCT band absorption of the $[Cu(dmphen)_2]^+$ to a known concentration of Cu^+ ions. The data points are the mean value over 2 independent measurements and the error bars are the standard deviation calculated over the same measurements.

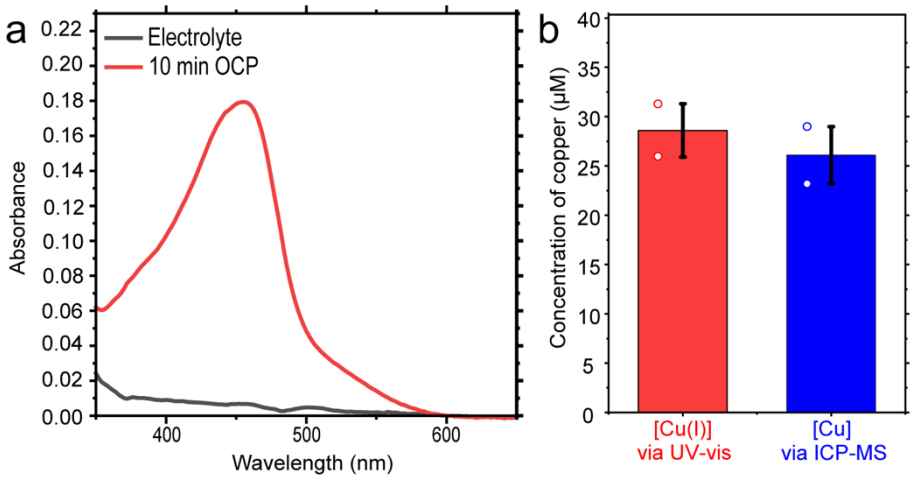

Supplementary Figure 5: (a) UV-Vis spectra of the dissolution of the copper species for Cu foil at OCP monitored after 10 min. (b) Cu concentration quantified from the same UV-Vis data and ex-situ ICP-MS. Data are the mean of two independent data points (showed in the graph) and the error bars are the calculated standard deviation.

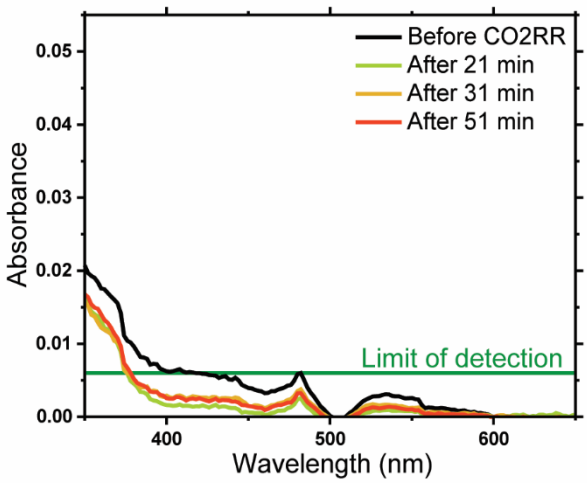

Supplementary Figure 6: Absorption spectra measured during CO_2RR at –1.1V vs RHE in a typical H-cell performed in the presence of 0.1mM dmphen. The electrolyte was sampled at different time during the course of the experiment.

Supplementary Note 3: Impact of the dmphen on the Cu dissolution

The optical detection studies were performed at ambient temperature (approximatively 25°C), at a concentration of Cu in solution in the micromolar range, at pH of 6.8 and at OCP potential of $+0.4V_{RHE}$. Under these conditions, the Cu Pourbaix diagram suggests the existence of an equilibrium between Cu_2O in condensed phase and Cu^{2+} in solution.[6] However, the experimental conditions presented in this study include CO_2 saturated in solution, which could possibly drive the equilibrium towards Cu^+. Of course, another possibility to consider is that the presence of the chelating ligand modifies this equilibrium. The experiments presented hereafter show that the impact of the dmphen on the copper dissolution is not significant under the conditions used for this study.

Comparison of the measurements using the UV-vis detection of the $[Cu(dmphen)_2]^+$ and *ex-situ* ICP-MS (Supplementary Figure 7) indicate that the ligand cannot chelate the Cu^+ intermediates when the concentration of the dmphen is too low (0.01 mM and less). However, the *ex-situ* ICP-MS still measures comparable amounts of copper. Thus, meaning that the addition of dmphen does not significantly alter the amount of copper that dissolves from the electrode.

Interestingly, it was found that adding dmphen to the aliquot taken after 10 minutes at OCP in a ligand-free solution does not bring back the signal of the dissolved copper in the detection via UV-vis spectroscopy (zero signal), but the ICP-MS measurements still account for similar amounts of copper (4.2µM). This observation suggests that the Cu^+ ions oxidize in the absence of the chelating ligand to form Cu^{2+} ions, which are not detectable by UV-vis.

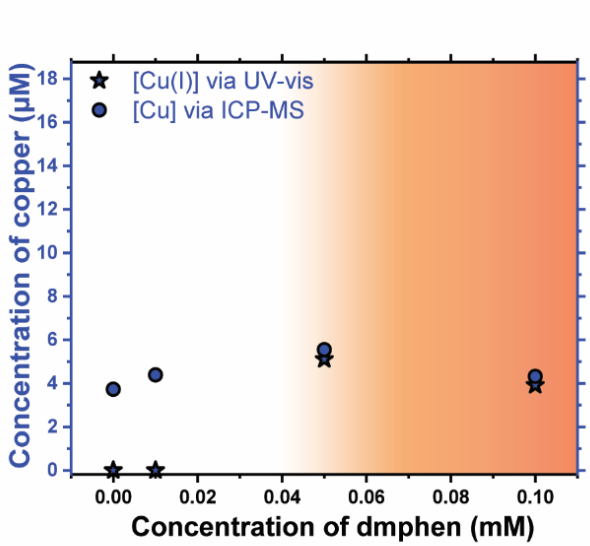

Supplementary Figure 7: Mass of all copper species dissolved measured by *ex-situ* ICP-MS and mass of Cu(I) dissolved measured by UV-Vis after 10 minutes at OCP versus the concentration of chelating ligand in solution. The concentration of Cu detected by ICP-MS is independent from the concentration of the ligand in solution which indicates no impact of the dmphen on the dissolution equilibrium. The data in this graph were acquired using drop casted copper catalyst. Data are the average of two independent experiments and the error bars are the calculated standard deviation.

Supplementary Note 4: Impact of dmphen on the catalytic properties and on the reconstruction of copper during CO_2RR

The effect of the dmphen on the catalytic properties and on the reconstruction of copper during CO_2RR was examined. As a reminder, the dmphen concentration used for the optical detection studies is 0.1 mM, which is the needed for a reliable acquisition of the optical signal. Supplementary Figure 8 indicates a drop in current density at this concentration of dmphen. This current drop suggests that the dmphen adsorbs on the Cu surface and blocks some of the available active sites, resulting in decreased catalyst activity. Concomitantly, the faradaic efficiency for hydrogen increases, which further confirms blockage of some reactive sites for the CO_2 conversion. Nevertheless, the main products methane, ethylene, and formate are still generated, indicating that the intrinsic selectivity of the Cu NPs is preserved in the presence of the ligand.

TEM images of the as-synthesized copper catalyst and of the catalyst after 1 h of CO_2RR without and with dmphen were also collected. Fig. S3.6 illustrates that the dmphen does not modify the morphology of the catalyst at OCP and does not interfere with the reconstruction into “scrambled” catalyst of the Cu NPs.

Altogether, these results indicate that the dmphen does not have a major impact on the intrinsic catalytic properties and reconstruction behavior during CO_2RR of the Cu NPs.

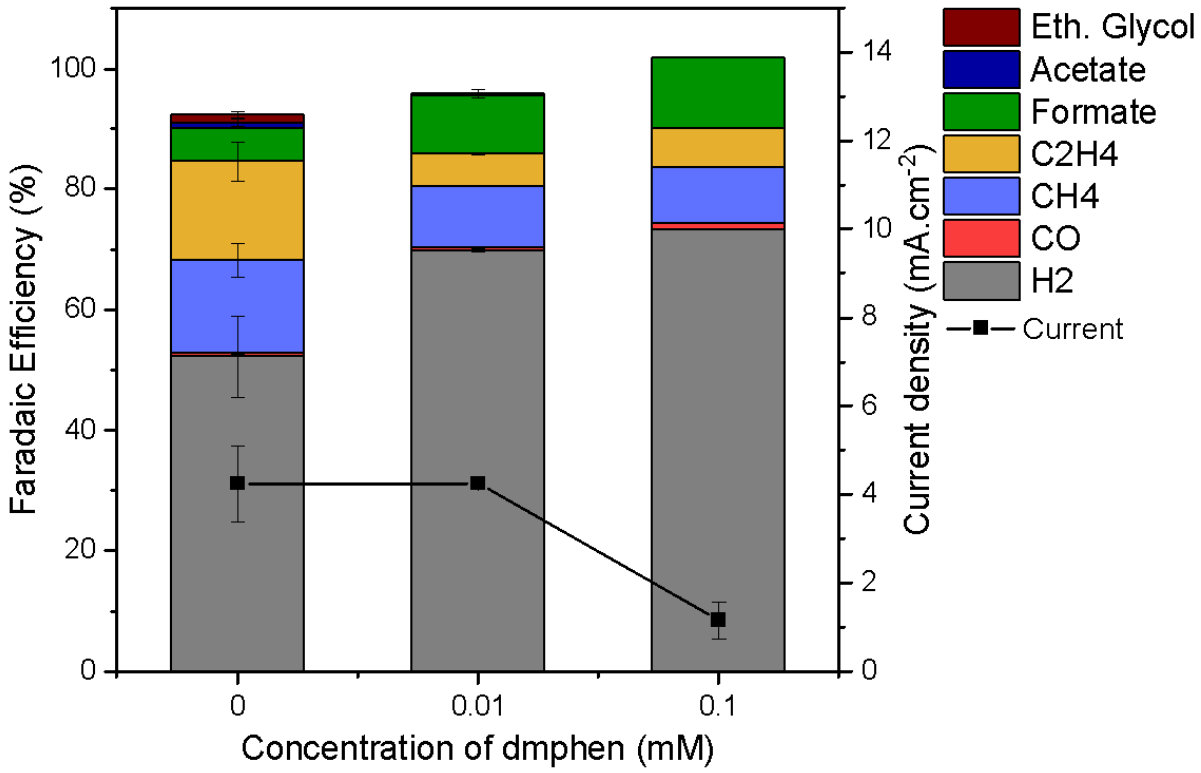

Supplementary Figure 8: Faradaic efficiency for different products and current density at different concentration of dmphen in the electrolyte for CO_2RR measurements performed at –1.1 V vs RHE. Data are the mean of three independent experiments and the error bars are the calculated standard deviation.

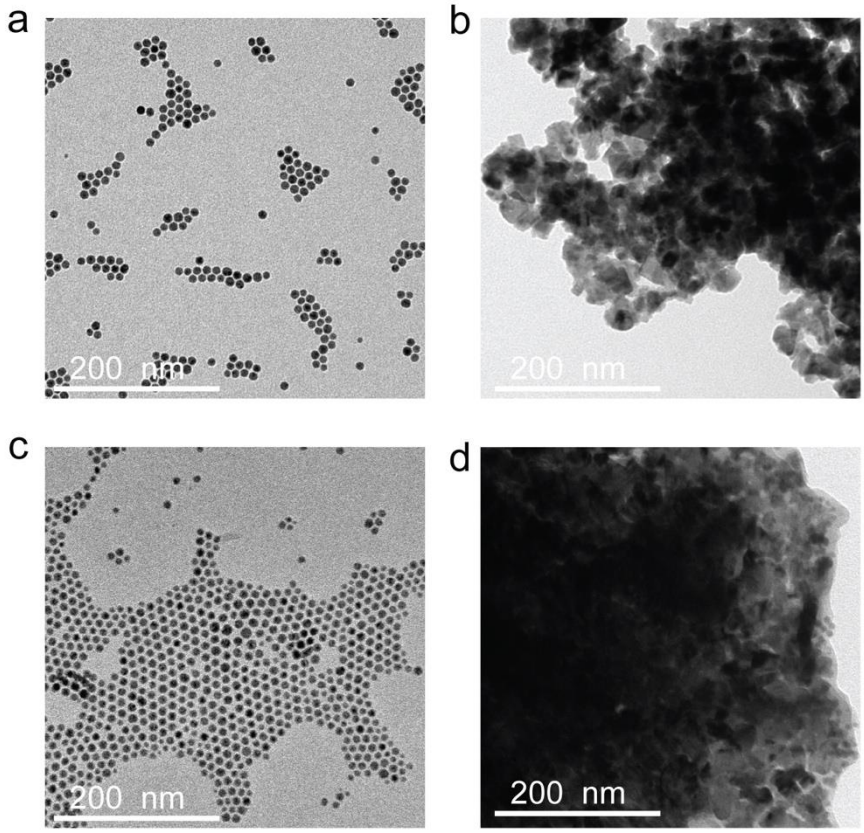

Supplementary Figure 9: TEM images of the copper catalyst (a) as synthesized, (b) after 1 h of CO_2RR at $-1.1V_{RHE}$ in 0.1 M $KHCO_3$, (c) after 1 h at OCP in 0.1 M $KHCO_3$+ 0.1 mM dmphen (d) after 1 h of CO_2RR at $-1.1V_{RHE}$ in 0.1 M $KHCO_3$+ 0.1 mM dmphen.

Supplementary Note 5: Effect of the dmphen on the Cu redox properties

To further confirm that the oxidation state of the Cu catalyst and its redox properties are not impacted by the presence of the chelating ligands in the electrolyte, in-situ XAS studies were performed.

X-ray Absorption Spectroscopy was performed at beamline BM31 at ESRF in a custom cell, used in previous campaigns from the group. The catalyst suspension was drop-casted onto a thin (2.5 × 2.5 × 0.5 mm3) glassy carbon (GC) support and a Kapton window allowed the X-rays to pass through. For the standards (*i.e.*, pressed pellets with the sample diluted in a light matrix such as boron nitride or cellulose to obtain an appropriate thickness), XAS was collected in transmission using ionization chambers for transmission detection. The *in-situ* measurements for the Cu NPs were carried out in fluorescence mode at an incident angle of approximately 45 degrees (Beam size 0.5 mm vertical and 8 mm horizontal). A Si(111) double crystal monochromator (DCM) was used to condition the beam from the bending magnet source. Fluorescence X-ray absorption near edge structure (XANES) spectra were acquired using a Vortex® single-element silicon drift detector (SDD) with XIA-Mercury digital electronics and a time-resolution of 3 min per spectrum. The Cu K-edge (8.9789 keV) was followed. The resulting XAS data were reduced and normalized using the Prestopronto package or PAXAS.

The main protocol for the measurements consisted of 0.2 V potential steps from OCP to –1 V vs RHE in the absence or in the presence of 0.1 mM dmphen. The dry sample corresponds to the sample measured before OCP as a reference. The data extracted from linear combination analysis of the XANES spectra, using standards of Cu, Cu_2O and CuO, are presented in Supplementary Figure 10. Overall, no statistically significant difference is observed in the redox changes of the Cu NPs during the application of the cathodic voltage under CO_2RR conditions without or with the dmphen.

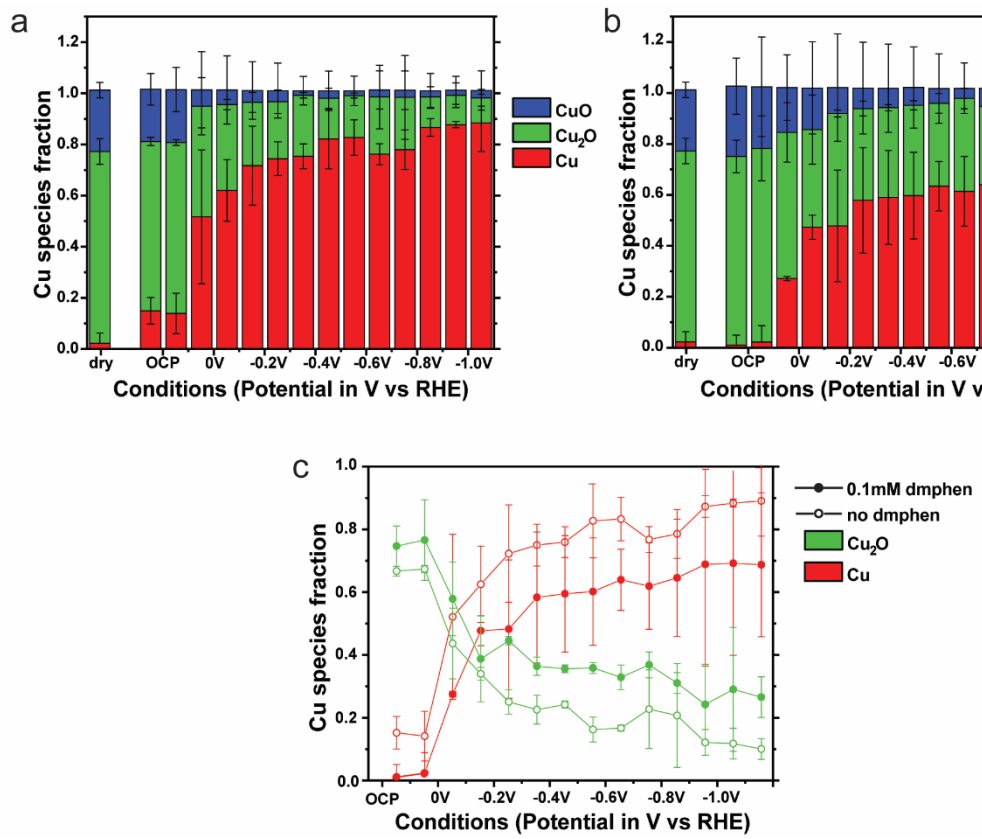

Supplementary Figure 10: Evolution of Cu species fraction of the Cu NPs from OCP to –1 V vs RHE without (a) and with (b) 0.1 mM dmphen. (c) Fractions of Cu_2O (green) and metallic Cu (red) as a function of the applied potential without (empty circles) and with (filled circles) dmphen. The data points are obtained by averaging two independent experiments and the error bars are the calculated standard deviation.

Computational details

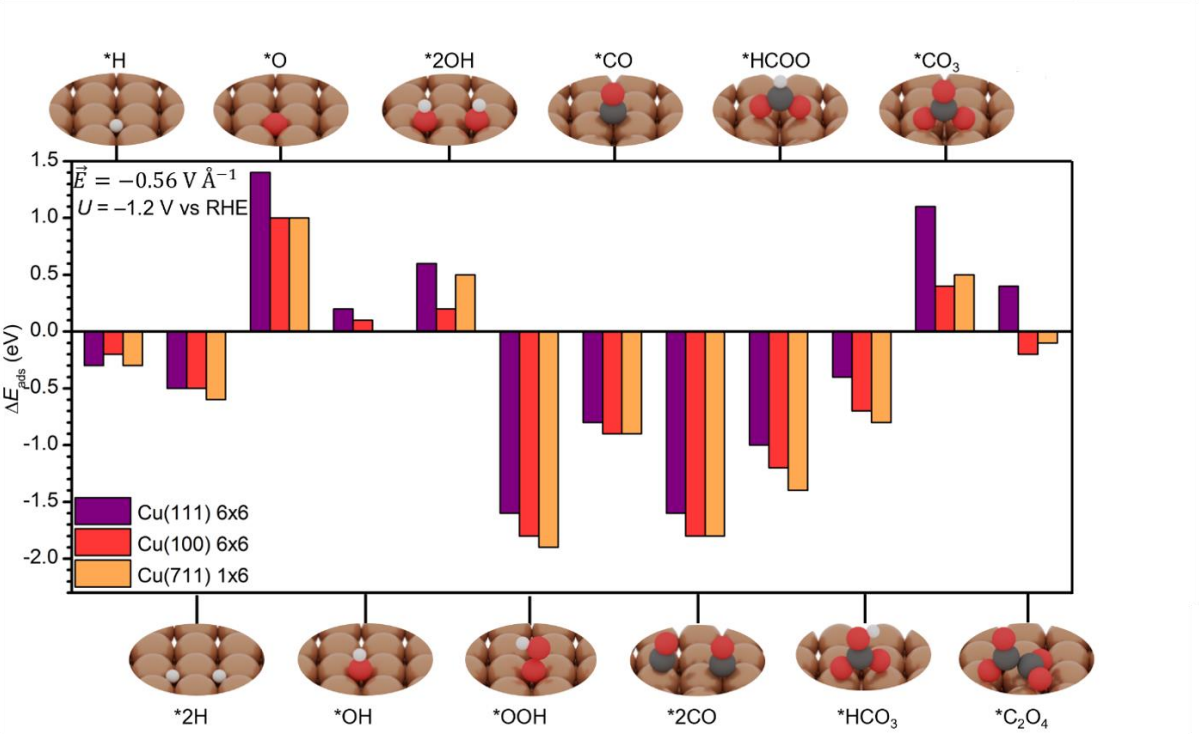

Supplementary Figure 11: DFT energies required to form different adsorbates along the HER, ORR, and CO_2R pathways (as shown in the insets) on Cu(111) (6×6) (θ = 0.03 ML, purple), Cu(100) 6×6 (θ = 0.03 ML, red), and Cu(711) (1×6) (θ = 0.04 ML, orange). CO_2(g), H_2(g), H_2O(g) were employed as energy references for all intermediates except *OOH, were H_2(g) and O_2(g) (corrected according to Ref.[7]) were employed instead.

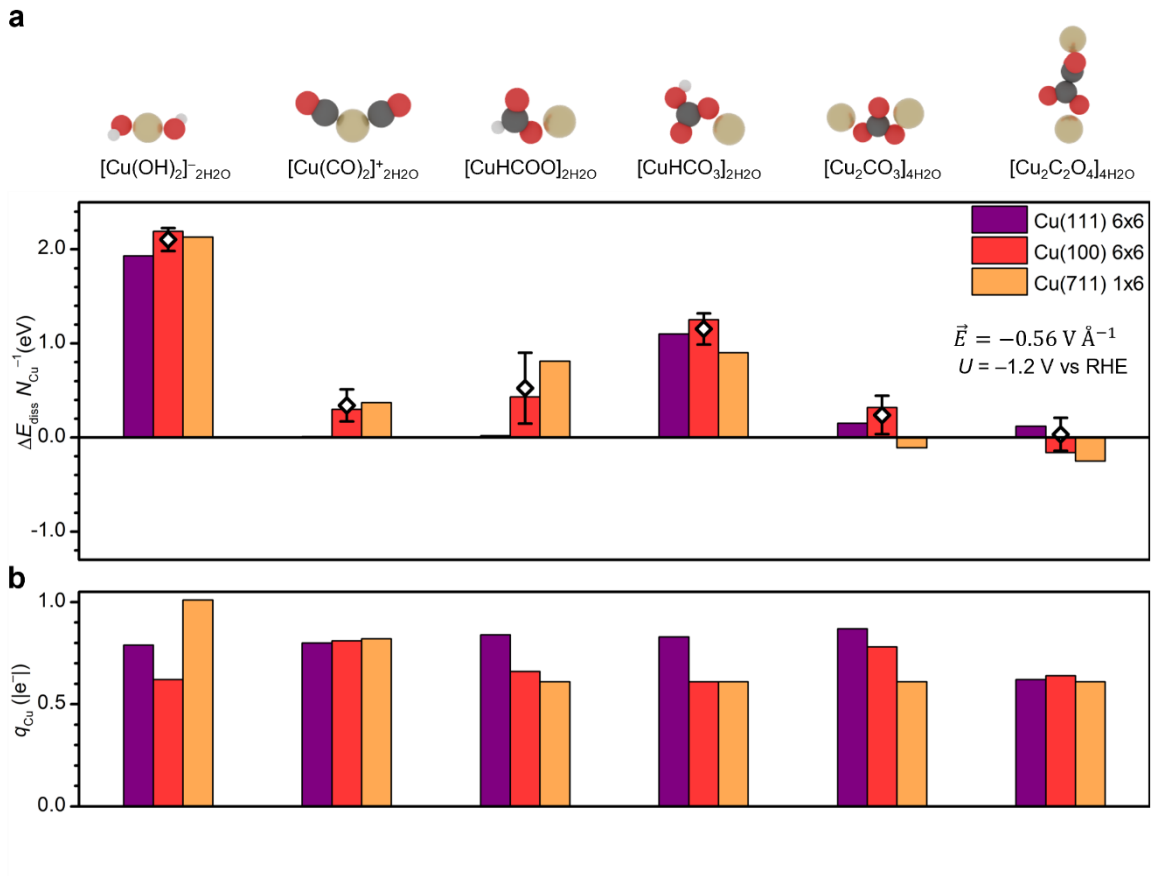

Supplementary Figure 12: (a) DFT energy required to form $[Cu^{+}L]_{aq}$ complexes with one surface atom from Cu(111) (6×6) (θ = 0.03 ML, purple), Cu(100) 6×6 (θ = 0.03 ML, red), and Cu(711) (1×6) (θ = 0.04 ML, orange) under an applied electric field of –0.56 V Å^{-1}, equivalent to –1.2 V vs RHE (see Methods). From left to right, ligands L = 2OH^{-}, 2CO, HCOO^{-}, HCO_3^{-}, CO_3^{2-}, $C_2O_4^{2-}$. The empty diamond symbols represent the mean of the energies estimated for each facet (reported in the bar plot); the error bars are the calculated standard deviation. (b) Cu Bader charges for $[Cu^{+}L]_{aq}$ complexes. When two Cu atoms were present, the reported value represents the mean of two Bader charges. The subscript indicates the number of H_2O ligands for each Cu complex, to complete the first solvation shell with four-coordination geometry.

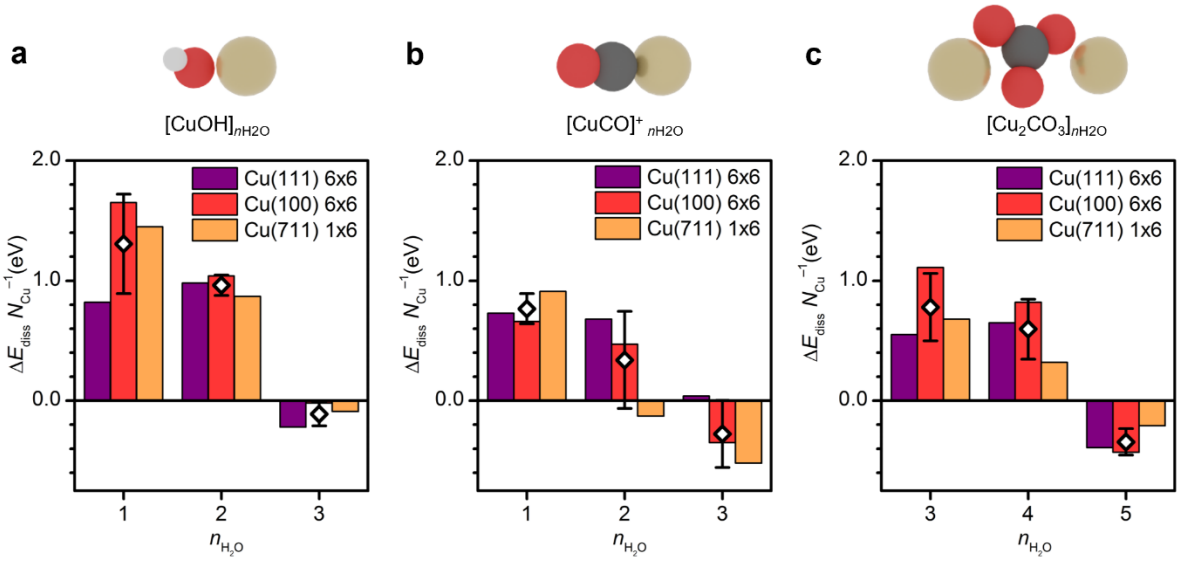

Supplementary Figure 13: DFT energy required to form (a) $[CuOH]_{n}H2O$, $[CuCO]^{+}{}_{n}H2O$, and $[CuCO_3]_{n}H2O$ complexes detaching one surface atom from Cu(111) 3×3 (θ = 0.11 ML, purple), Cu(100) 3×3 (θ = 0.11 ML, red), and Cu(711) 1×3 (θ = 0.06 ML, orange) at –1.2 V vs RHE and different number of water molecules within the first solvation shell of the complexes. The empty diamond symbols represent the mean of the energies estimated for each facet (reported in the bar plot); the error bars are the calculated standard deviation.

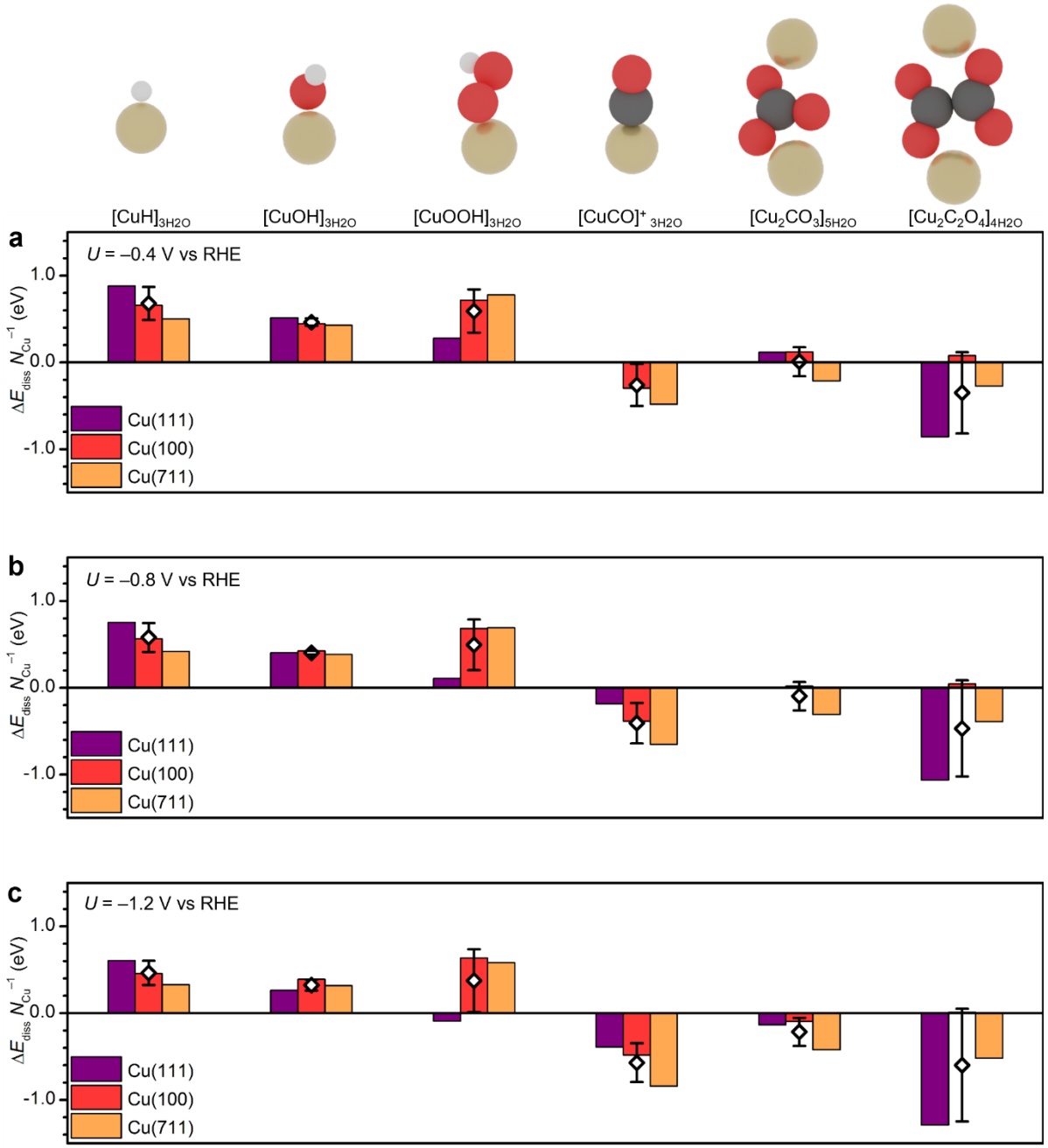

Supplementary Figure 14: DFT energy required to form $[Cu^{+}L]_{aq}$ complexes detaching one surface atom from Cu(111) (6×6) (θ = 0.03 ML, purple), Cu(100) 6×6 (θ = 0.03 ML, red), and Cu(711) (1×6) (θ = 0.04 ML, orange) under an applied electric potential of (a) –0.4 V vs RHE, (b) –0.8 V vs RHE, and (a) –1.2 V vs RHE. From left to right, ligands L = H, OH^{-}, OOH^{-}, CO, CO_3^{2-}, $C_2O_4^{2-}$. The empty diamond symbols represent the mean of the energies estimated for each facet (reported in the bar plot); the error bars are the calculated standard deviation.

Supplementary Table 1: DFT energy required to form $[Cu^{+}L]_{nH2O}$ complexes detaching one surface atom from Cu(111) 6×6, Cu(100) 6×6, and Cu(711) 1×6 at applied electric potentials –0.4 V vs RHE and –0.8 V vs RHE

ΔE_{diss}	U = –0.4 V vs RHE			U = –0.8 V vs RHE		
System	**Cu(111)**	**Cu(100)**	**Cu(711)**	**Cu(111)**	**Cu(100)**	**Cu(711)**
$[CuH]_{3H2O}$	+0.9	+0.7	+0.5	+0.8	+0.6	+0.4
$[CuOH]_{3H2O}$	+0.5	+0.4	+0.4	+0.4	+0.4	+0.4
$[Cu(OH)_2]^{-}{}_{2H2O}$	+2.5	+2.3	+2.3	+2.3	+2.3	+2.2
$[CuOOH]_{3H2O}$	+0.3	+0.7	+0.8	+0.1	+0.7	+0.7
$[CuCO]^{+}{}_{3H2O}$	+0.0	–0.3	–0.5	–0.2	–0.4	–0.7
$[Cu(CO)_2]^{+}{}_{2H2O}$	+0.7	+0.8	+0.9	+0.4	+0.6	+0.6
$[CuHCOO]_{2H2O}$	+0.3	+0.6	+0.8	+0.2	+0.5	+0.8
$[CuHCO_3]_{2H2O}$	+1.3	+1.2	+1.0	+1.2	+1.2	+0.9
$[Cu_2CO_3]_{5H2O}$ (Fig. 5c)	+0.1	+0.1	–0.2	+0.0	+0.0	–0.3
$[Cu_2CO_3]_{4H2O}$ (Fig, S4.2)	+0.4	+0.5	+0.0	+0.3	+0.4	+0.0
$[Cu_2C_2O_4]_{4H2O}$ (Fig. S4.2)	+0.4	+0.1	–0.1	+0.3	+0.0	–0.2
$[Cu_2C_2O_4]_{4H2O}$ (Fig. 5c)	–0.9	+0.1	–0.3	–1.1	+0.0	–0.4
$[Cu(dmphen)_2]^{+}$	–0.5	–0.9	–0.6	–0.8	–1.1	–0.8

Supplementary Table 2: DFT energy to form adsorbates on Cu(111) 6×6, Cu(100) 6×6, and Cu(711) 1×6 at applied electric potentials –0.4 V vs RHE and –0.8 V vs RHE. CO_2(g), H_2(g), H_2O(g), and dmphen(g) were employed as energy references for all intermediates except *OOH, were H_2(g) and O_2(g) (corrected according to Ref.[7]) were employed instead.

ΔE_{ads}	U = –0.4 V vs RHE			U = –0.8 V vs RHE		
System	**Cu(111)**	**Cu(100)**	**Cu(711)**	**Cu(111)**	**Cu(100)**	**Cu(711)**
*H	–0.3	–0.2	–0.3	–0.3	–0.2	–0.3
*2H	–0.5	–0.5	–0.6	–0.5	–0.5	–0.6
*O	+1.3	+1.0	+1.0	+1.4	+1.0	+1.0
*OH	+0.3	+0.1	+0.0	+0.2	+0.1	+0.0
*2OH	+0.7	+0.3	+0.4	+0.6	+0.3	+0.4
*OOH	–0.3	–0.5	–1.1	–0.9	–1.0	–1.4
*CO	–0.9	–1.0	–0.9	–0.9	–0.9	–0.9
*2CO	–1.6	–1.8	–1.8	–1.6	–1.8	–1.8
*OCHO	–0.9	–1.2	–1.4	–1.0	–1.2	–1.4
*HCO_3	–0.4	–0.7	–0.8	–0.4	–0.7	–0.8
*CO_3	+1.0	+0.2	+0.3	+1.1	+0.3	+0.4
*C_2O_4	+0.3	–0.4	–0.3	+0.4	–0.3	–0.2
*2dmphen	–1.1	–1.1	–1.2	–1.2	–1.2	–1.3

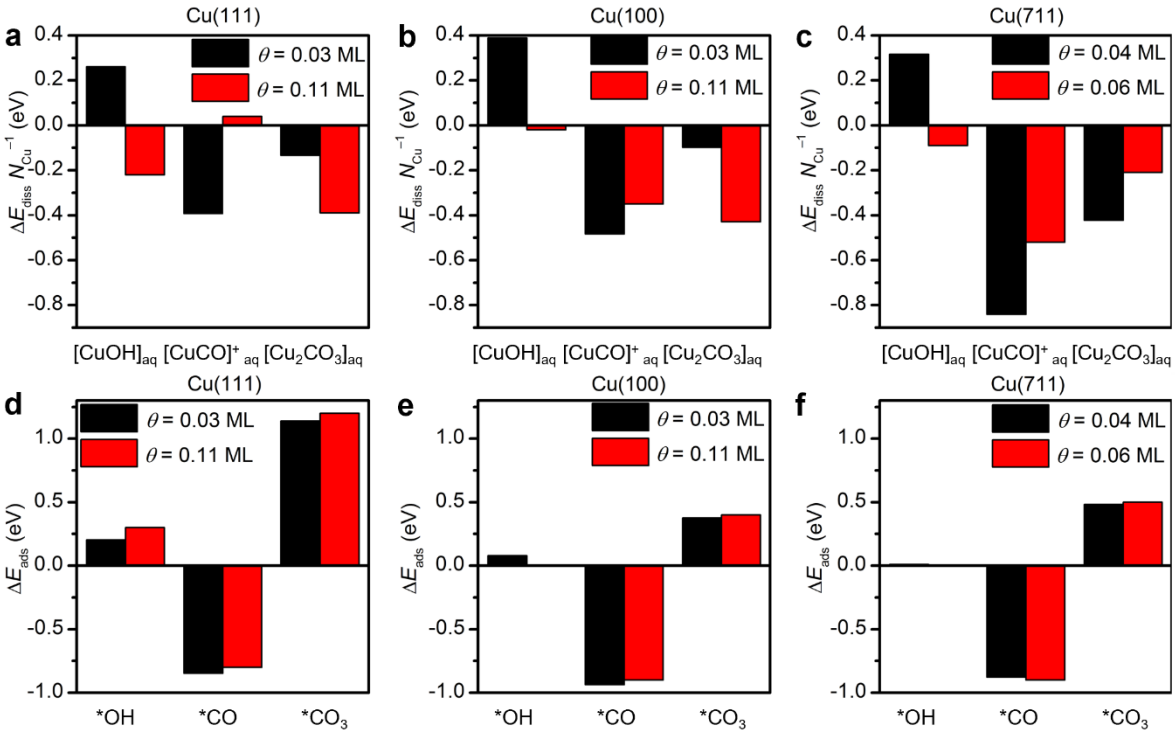

Supplementary Figure 15: DFT energy required to form $[Cu(OH)]_{3H2O}$, $[Cu(CO)]^{+}_{3H2O}$ and $[Cu_2CO_3]_{5H2O}$ complexes detaching one surface atom from (a) Cu(111), (b) Cu(100), and (c) Cu(711) at different surface coverages θ under an applied electric field of –0.56 V Å^{-1}, equivalent to –1.2 V vs RHE (see Methods). Formation energies for adsorbed *OH, *CO, and $*CO_3$ on (d) Cu(111), (e) Cu(100), and (f) Cu(711) at different coverages θ and electric potential –1.2 V vs RHE.

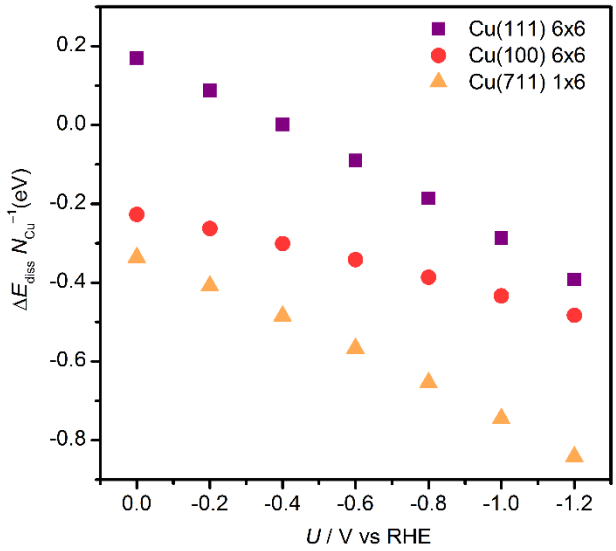

Supplementary Figure 16: DFT energy required to form a $[Cu(CO)]^{+}{}_{3H2O}$ complex detaching one surface atom from Cu(111) 6×6 (purple), Cu(100) 6×6 (red), and Cu(711) 1×6 (orange) vs applied potential vs RHE.

Supplementary Table 3: Total Bader charges for Cu(I) complexes formed through Cu dissolution from Cu(111), Cu(100), and Cu(711). The subscript indicates the number of H_2O ligands for each Cu atom.

	q **(|e⁻|)**		
Complex	**Cu(111)**	**Cu(100)**	**Cu(711)**
$[CuH]_{3H2O}$	+0.1	0.0	0.0
$[CuOH]_{3H2O}$	0.0	0.0	0.0
$[Cu(OH)_2]^{-}{}_{2H2O}$	–0.4	–0.7	–0.3
$[CuOOH]_{3H2O}$	+0.1	0.0	0.0
$[CuCO]^{+}{}_{3H2O}$	+0.8	+0.7	+0.8
$[Cu(CO)_2]^{+}{}_{2H2O}$	+1.0	+1.0	+1.0
$[CuHCOO]_{2H2O}$	0.0	0.0	0.0
$[CuHCO_3]_{2H2O}$	+0.1	+0.1	0.0
$[Cu_2CO_3]_{5H2O}$ (Fig. 5c)	+0.2	0.0	0.0
$[Cu_2CO_3]_{4H2O}$ (Fig, S14)	+0.7	+0.2	0.0
$[Cu_2C_2O_4]_{4H2O}$ (Fig. S14)	+0.8	+0.4	0.0
$[Cu_2C_2O_4]_{4H2O}$ (Fig. 5c)	0.0	0.0	0.0
$[Cu(dmphen)_2]^{+}$	+0.8	+0.9	+0.8

Supplementary Note 6: The role of the adsorption of dimethyl phenanthroline on the reconstruction process during CO_2RR.

Supplementary Figure 17a indicates that the dissolution of copper as $[Cu(dmphen)_2]^+$ is thermodynamically favorable. Yet, experimental data show that the addition of dmphen in solution does not significantly impact Cu dissolution (Supplementary Note 3), at least at dmphen concentration ≤ 0.1mM. We note that the dissolution rates are affected not only by thermodynamics but also by kinetics and mass transport effects, which density functional theory simulations disregard. Given the higher concentrations of CO, carbonate, and oxalates at the surface under CO_2RR conditions, any dissolution processes resulting from these species would anyway have higher rates than that related to dmphen, due to the limited diffusion of the latter compound.

Furthermore, Supplementary Figure 17b evidences that the conversion of $[CuCO]^+_{aq}$ to $[Cu(dmphen)_2]^+$, as written in Supplementary Equation 1, is highly exothermic (< –2.0 eV), thus confirming that Cu complexes, once in solution, will readily convert to $[Cu(dmphen)_2]^+$.

$$[CuCO]^+_{aq} + 2dmphen \rightarrow [Cu(dmphen)_2]^+ + CO \qquad \text{Supplementary Equation 1}$$

Copper-carbonyl exhibits the most exothermic dissolution energy for any considered Cu facet, thus insights into its conversions can be extended to the other, less favorable, species. The stabilized intermediate in the form of $[Cu(dmphen)_2]^+$ then accumulates in the electrolyte, which facilitates its detection as depicted in Supplementary Figure 17c.

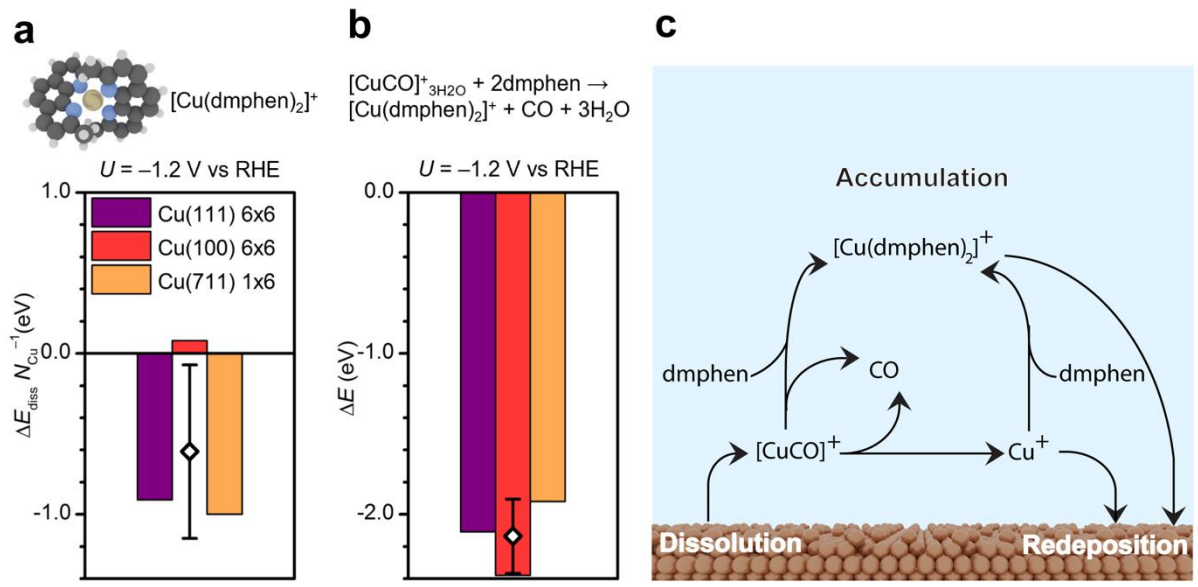

Supplementary Figure 17:(a) DFT energy required to form $[Cu(dmphen)_2]^+$ with one surface atom from Cu(111) (6×6) (θ = 0.03 ML, purple), Cu(100) 6×6 (θ = 0.03 ML, red), and Cu(711) (1×6) (θ = 0.04 ML, orange) under an applied electric field of –0.56 V $Å^{-1}$, equivalent to –1.2 V vs RHE (see Methods). (b) DFT energy associated to conversion of $[CuCO]^+_{aq}$ to $[Cu(dmphen)_2]^+$ on Cu(111) 6×6 (purple, θ = 0.03 ML), Cu(100) 6×6 (red, θ = 0.03 ML), and Cu(711) 6×6 (orange, θ = 0.04 ML) under applied electric field of –0.56 V Å–1, equivalent to –1.2 V vs RHE (see Methods). DFT energy for CO(g) has been calculated employing CO_2(g), H_2(g), H_2O(g) as energy reference and its experimental enthalpy of formation. The subscript aq indicates between 1 and 3 H_2O ligands for each Cu atom, to achieve a four-coordination geometry. The empty diamond symbols represent the mean of the energies estimated for each facet (reported in the bar plot); the error bars are the calculated standard deviation. (c) Sketch for dissolution – redeposition cycle and formation of $[Cu(dmphen)_2]^+$ complexes.

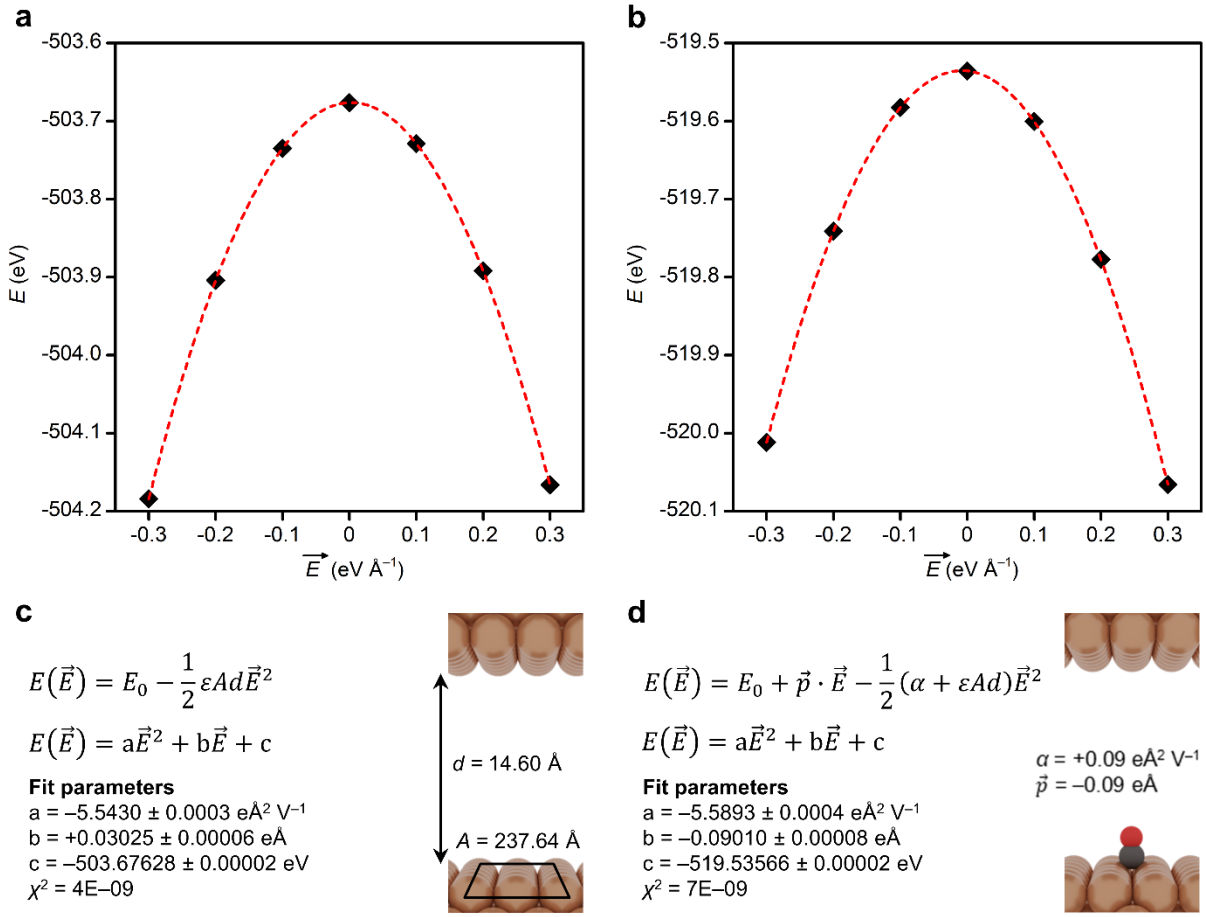

Supplementary Figure 18: DFT energy for (a) clean Cu(100) 6×6 and (b) CO adsorbed on Cu(100) 6×6 versus applied electric field. Data points have been fitted through Equation 4, reported in panels (c) and (d) for both cases together with the fitting parameters. E_0: DFT energy at 0 V Å^{-1} applied electric field, ε: dielectric permittivity of the medium, d: medium thickness, A: electrode area, $\vec{p}$: electric dipole of the intermediate, α: polarizability of the intermediate. The dielectric permittivity of the medium estimated from fitting parameters in panel (c) is equivalent to 5.12E–12 F m^{-1}, in line with the standard value for vacuum (8.85E–12 F m^{-1}).

Supplementary Table 4: Quadratic fit parameters of DFT energies versus electric field for clean surface (*), adsorbates, and Cu complexes on Cu(111) 6×6, as reported in Supplementary Equation 2. $\vec{p}$ is the electric dipole moment of the intermediate, α its polarizability, ε the dielectric permittivity of the medium (electrolyte), A the electrode surface area, and d the thickness of the dielectric double layer. The subscript indicates the number of H_2O ligands.

$a = -\frac{1}{2}(\alpha + \varepsilon A d)$; $b = \vec{p}$; $c = E(\vec{E} = 0\ V\ Å^{-1})$. Supplementary Equation 2

System	a (eÅ² V⁻¹)	b (eÅ)	c (eV)	χ^2
*	–5.3187 ± 0.0002	+0.01971 ± 0.00003	–514.463738 ± 0.000009	1.0E–09
*H	–5.3131 ± 0.0002	+0.01263 ± 0.00003	–518.092056 ± 0.000011	1.3E–09
*2H	–5.3141 ± 0.0002	–0.00358 ± 0.00004	–521.661391 ± 0.000012	2E–09
*O	–5.3146 ± 0.0004	–0.09610 ± 0.00008	–521.01126 ± 0.00002	7E–09
*OH	–5.3424 ± 0.0003	+0.23523 ± 0.00005	–525.275096 ± 0.000014	2E–09
*2OH	–5.36258 ± 0.00015	+0.39630 ± 0.00003	–535.991480 ± 0.000008	7E–10
*OOH	–5.4059 ± 0.0003	+0.01475 ± 0.00005	–529.32344 ± 0.00002	3E–09
*CO	–5.3741 ± 0.0006	–0.09623 ± 0.00010	–530.19688 ± 0.00003	1.1E–08
*2CO	–5.4310 ± 0.0009	–0.1714 ± 0.0002	–545.80239 ± 0.00005	3E–08
*OCHO	–5.4115 ± 0.0007	+0.05886 ± 0.00012	–541.41017 ± 0.00004	2E–08
*HCO_3	–5.4510 ± 0.0009	+0.0273 ± 0.0002	–548.58202 ± 0.00005	3E–08
*CO_3	–5.441 ± 0.002	–0.6712 ± 0.0003	–544.03344 ± 0.00010	1.2E–07
*C_2O_4	–5.500 ± 0.002	–0.7455 ± 0.0003	–559.62965 ± 0.00010	1.3E–07
*2dmphen	–6.2481 ± 0.0004	+1.11116 ± 0.00007	–891.11105 ± 0.00002	6.0E–09
$[CuH]_{3H2O}$	–5.833 ± 0.007	+0.5957 ± 0.0013	–558.5958 ± 0.0004	2E–06
$[CuOH]_{3H2O}$	–6.21 ± 0.04	+0.444 ± 0.007	–566.171 ± 0.002	5E–05
$[Cu(OH)_2]^-_{2H2O}$	–8.7 ± 0.6	–0.36 ± 0.10	–560.89 ± 0.02	4E–03
$[CuOOH]_{3H2O}$	–6.19 ± 0.02	+0.730 ± 0.004	–570.3496 ± 0.0009	6E–06
$[CuCO]^+_{3H2O}$	–5.898 ± 0.012	+0.931 ± 0.002	–571.6661 ± 0.0006	3E–06
$[Cu(CO)_2]^+_{2H2O}$	–6.886 ± 0.002	+1.35241 ± 0.00036	–571.45405 ± 0.00011	1.4E–07
$[CuHCOO]_{2H2O}$	–6.09 ± 0.09	+0.495 ± 0.016	–567.389 ± 0.005	3E–04
$[CuHCO_3]_{2H2O}$	–6.13 ± 0.07	+0.250 ± 0.013	–574.689 ± 0.004	1.2E–04
$[Cu_2CO_3]_{5H2O}$ (Fig. 5c)	–6.1 ± 0.2	+0.52 ± 0.04	–613.169 ± 0.004	9E–05
$[Cu_2CO_3]_{4H2O}$ (Fig, S4.2)	–6.26 ± 0.12	+0.43 ± 0.02	–598.410 ± 0.006	5E–04
$[Cu_2C_2O_4]_{4H2O}$ (Fig. S4.2)	–6.37 ± 0.12	+0.48 ± 0.02	–613.282 ± 0.007	4E–04
$[Cu_2C_2O_4]_{4H2O}$ (Fig. 5c)	–6.53 ± 0.08	+1.609 ± 0.015	–613.897 ± 0.003	8E–05
$[Cu(dmphen)_2]^+$	–7.16 ± 0.06	+2.3186 ± 0.0097	–891.039 ± 0.003	1.1E–04

Supplementary Table 5: Quadratic fit parameters of DFT energies versus the electric field for clean surface (*), adsorbates, and Cu complexes on Cu(100) (6×6), as reported in Supplementary Equation 2. The subscript indicates the number of H_2O ligands.

System	a (eÅ^2 V^{-1})	b (eÅ)	c (eV)	χ^2
*	–5.5430 ± 0.0003	+0.03025 ± 0.00006	–503.67628 ± 0.00002	4E–09
*H	–5.5320 ± 0.0004	+0.01699 ± 0.00006	–507.29452 ± 0.00002	4E–09
*2H	–5.5282 ± 0.0003	+0.00538 ± 0.00005	–510.889349 ± 0.000014	2E–09
*O	–5.5245 ± 0.0005	–0.05094 ± 0.00009	–510.66655 ± 0.00003	9E–09
*OH	–5.5515 ± 0.0003	+0.21297 ± 0.00005	–514.67835 ± 0.00002	3E–09
*2OH	–5.5635 ± 0.0005	+0.37640 ± 0.00009	–525.63825 ± 0.00003	8E–09
*OOH	–5.6021 ± 0.0004	+0.02258 ± 0.00007	–518.79142 ± 0.00002	6E–09
*CO	–5.5893 ± 0.0004	–0.09010 ± 0.00008	–519.53566 ± 0.00002	7E–09
*2CO	–5.6503 ± 0.0007	–0.12945 ± 0.00013	–535.24808 ± 0.00004	2E–08
*OCHO	–5.6187 ± 0.0009	+0.00375 ± 0.00015	–530.94888 ± 0.00005	3E–08
*HCO_3	–5.6524 ± 0.0009	+0.05151 ± 0.00015	–538.13163 ± 0.00005	3E–08
*CO_3	–5.639 ± 0.002	–0.6935 ± 0.0003	–534.05181 ± 0.00010	1.2E–07
*C_2O_4	–5.6568 ± 0.0014	–0.6293 ± 0.0002	–549.60180 ± 0.00007	6E–08
*2dmphen	–6.5831 ± 0.0008	+1.05704 ± 0.00014	–880.12117 ± 0.00005	1.5E–08
$[CuH]_{3H2O}$	–5.97 ± 0.04	+0.398 ± 0.006	–548.198 ± 0.002	4E–05
$[CuOH]_{3H2O}$	–6.07 ± 0.06	–0.027 ± 0.010	–555.724 ± 0.003	1.0E–04
$[Cu(OH)_2]^-_{2H2O}$	–7.2 ± 0.2	–0.46 ± 0.04	–550.697 ± 0.009	7E–04
$[CuOOH]_{3H2O}$	–5.97 ± 0.07	+0.026 ± 0.015	–559.5536 ± 0.0015	1.2 E–05
$[CuCO]^+_{3H2O}$	–5.920 ± 0.002	+0.3103 ± 0.0003	–561.84283 ± 0.00010	1.3E–07
$[Cu(CO)_2]^+_{2H2O}$	–6.730 ± 0.003	+0.8573 ± 0.0005	–561.28261 ± 0.00015	3E–07
$[CuHCOO]_{2H2O}$	–5.9241 ± 0.0007	+0.45337 ± 0.00013	–557.95545 ± 0.00003	6E–09
$[CuHCO_3]_{2H2O}$	–5.860 ± 0.009	–0.4428 ± 0.0015	–564.9548 ± 0.0003	8E–07
$[Cu_2CO_3]_{5H2O}$ (Fig. 5c)	–6.538 ± 0.007	+0.1625 ± 0.0014	–603.7588 ± 0.0004	1.3E–06
$[Cu_2CO_3]_{4H2O}$ (Fig, S4.2)	–6.83 ± 0.15	–0.06 ± 0.03	–588.781 ± 0.003	6E–05
$[Cu_2C_2O_4]_{4H2O}$ (Fig. S4.2)	–6.187 ± 0.006	+0.6988 ± 0.0014	–604.26974 ± 0.00014	1.0E–07
$[Cu_2C_2O_4]_{4H2O}$ (Fig. 5c)	–5.72 ± 0.11	–0.15 ± 0.02	–605.506 ± 0.006	3E–04
$[Cu(dmphen)_2]^+$	–7.62 ± 0.07	+2.289 ± 0.011	–880.567 ± 0.003	1.5E–04

Supplementary Table 6: Quadratic fit parameters of DFT energies versus the electric field for clean surface (*), surface adsorbates, and Cu complexes on Cu(711) (1×6), as reported in Supplementary Equation 2. The subscript indicates the number of H_2O ligands.

System	a (eÅ^2 V^{-1})	b (eÅ)	c (eV)	χ^2
*	–3.7509 ± 0.0002	–0.01824 ± 0.00003	–338.028505 ± 0.000009	9E–10
*H	–3.7448 ± 0.0002	–0.03016 ± 0.00004	–341.654215 ± 0.000012	2E–09
*2H	–3.7424 ± 0.0003	–0.04556 ± 0.00005	–345.276848 ± 0.000014	3E–09
*O	–3.7361 ± 0.0004	–0.11667 ± 0.00007	–344.97482 ± 0.00002	6E–09
*OH	–3.7706 ± 0.0004	–0.04490 ± 0.00008	–349.18592 ± 0.00002	6E–09
*2OH	–3.7937 ± 0.0007	–0.10232 ± 0.00012	–359.94491 ± 0.00004	2E–08
*CO	–3.8375 ± 0.0008	–0.12821 ± 0.00014	–353.79931 ± 0.00004	2E–08
*OOH	–3.8435 ± 0.0008	–0.0069 ± 0.0002	–353.21613 ± 0.00004	2E–08
*2CO	–3.9561 ± 0.0011	–0.1567 ± 0.0002	–369.56011 ± 0.00006	4E–08
*OCHO	–3.8633 ± 0.0010	–0.0940 ± 0.0002	–365.43542 ± 0.00005	4E–08
*HCO_3	–3.9036 ± 0.0012	–0.1230 ± 0.0002	–372.62334 ± 0.00007	5E–08
*CO_3	–3.878 ± 0.002	–0.7807 ± 0.0004	–368.26064 ± 0.00013	2E–07
*C_2O_4	–3.947 ± 0.003	–0.9501 ± 0.0005	–383.68417 ± 0.00014	2E–07
*2dmphen	–4.870 ± 0.004	+0.9712 ± 0.0006	–714.7154 ± 0.0002	4E–07
$[CuH]_{3H2O}$	–4.14 ± 0.04	+0.285 ± 0.006	–382.738 ± 0.002	4E–05
$[CuOH]_{3H2O}$	–4.30 ± 0.07	–0.075 ± 0.012	–390.235 ± 0.004	2E–04
$[Cu(OH)_2]^-_{2H2O}$	–4.79 ± 0.08	–0.358 ± 0.013	–384.966 ± 0.004	2E–04
$[CuOOH]_{3H2O}$	–4.56 ± 0.09	+0.11 ± 0.02	–393.933 ± 0.004	2E–04
$[CuCO]^+_{3H2O}$	–4.38 ± 0.02	+0.742 ± 0.003	–395.7242 ± 0.0010	1.2E–05
$[Cu(CO)_2]^+_{2H2O}$	–4.883 ± 0.002	+0.8795 ± 0.0004	–395.59100 ± 0.00012	2E–07
$[CuHCOO]_{2H2O}$	–4.03 ± 0.02	–0.214 ± 0.003	–392.5415 ± 0.0009	1.0E–05
$[CuHCO_3]_{2H2O}$	–4.06 ± 0.02	–0.035 ± 0.004	–399.5167 ± 0.0011	2E–05
$[Cu_2CO_3]_{5H2O}$ (Fig. 5c)	–4.96 ± 0.08	–0.156 ± 0.013	–438.618 ± 0.004	2E–04
$[Cu_2CO_3]_{4H2O}$ (Fig, S4.2)	–4.65 ± 0.05	–0.325 ± 0.008	–424.559 ± 0.003	8E–05
$[Cu_2C_2O_4]_{4H2O}$ (Fig. S4.2)	–4.33 ± 0.04	+0.183 ± 0.007	–438.973 ± 0.002	6E–05
$[Cu_2C_2O_4]_{4H2O}$ (Fig. 5c)	–4.46 ± 0.09	+0.450 ± 0.015	–440.248 ± 0.005	3E–04
$[Cu(dmphen)_2]^+$	–5.769 ± 0.010	+1.637 ± 0.002	–715.0274 ± 0.0005	4E–06

Supplementary References:

1. Speck, F. D. & Cherevko, S. Electrochemical copper dissolution: A benchmark for stable CO2 reduction on copper electrocatalysts. *Electrochem. commun.* **115**, 106739-106743.

2. Armaroli, N. Photoactive mono- and polynuclear Cu(I)-phenanthrolines. A viable alternative to Ru(II)-polypyridines? *Chem. Soc. Rev.* **30**, 113-124 (2001).

3. Pallenberg, A. J., Koenig, K. S. & Barnhartlb, D. M. Synthesis and Characterization of Some Copper(I) Phenanthroline Complexes. *Inorg. Chem* **34**, 2833–2840 (1995).

4. Ruthkosky, M., Kelly, C. A., Castellano, F. N. & Meyer, G. J. Electron and energy transfer from Cu I MLCT excited states, *Coordination Chem. Rev.* **171,** 309-322 (1998).

5. Magni, M., Colombo, A., Dragonetti, C. & Mussini, P. Steric vs electronic effects and solvent coordination in the electrochemistry of phenanthroline-based copper complexes. *Electrochimica Acta* **141**, 324–330 (2014).

6. Beverskog, B. & Puigdomenech, I. Revised Pourbaix Diagrams for Copper at 25 to 300°C. *Journal of The Electrochemical Society* **144**, 10, 3476-83 (1997).

7. Sargent, E., Illas, F., Rodríguez, P. & Calle-Vallejo, F. Importance of the gas-phase error correction for O_2 when using DFT to model the oxygen reduction and evolution reactions. *J. Electroanal. Chem.* **896**, (2021).